A Pathway to the Athermal Impact Initiation of Energetic Azides

Adam A.L. Michalchuk,[1,2] Peter T. Fincham,[3] Peter Portius,[4] Colin R. Pulham[1,2] and Carole A. Morrison[1*]

[1] EaStChem School of Chemistry and Centre for Science at Extreme Conditions, University of Edinburgh, Edinburgh, EH9 3FJ, UK.

[2] EPSRC Centre for Continuous Manufacturing and Crystallisation (CMAC), United Kingdom

[3] Defence Science and Technology Laboratory (DSTL), Porton Down, Salisbury, Wiltshire, SP4 0JG, UK.

[4] Department of Chemistry, University of Sheffield, Western Bank, Sheffield, S3 7HF, UK

S1. Crystal Structures and Structural Optimisation Criteria

All input structures were taken from the ICSD database, or published literature data, as indicated in Table S1. For calculations performed in CASTEP v16,[1] structures were converged using the GGA functional of Perdew-Burke-Ernzerhof (PBE)[2] with dispersion corrections as outlined in Table S1. Dispersion corrections were chosen so as to yield reasonable unit cell parameters on structural relaxation, Section S1.2. The 00PBE_OP norm-conserving pseudopotentials were used with a plane wave kinetic energy cur-off of 1800 eV. The optgg1 pseudopotential was used for the Zn atom. The electronic structure was sampled on a Monkhorst-Pack (MP) grid,[3] with k-point spacing of no more than 0.05 Å^{-1}, Table S1. Geometry optimisation convergence criteria are given in Table S1. Note that tighter convergence was required to ensure no imaginary phonons in the Zn material. Fully optimised structures were used for subsequent phonon calculations using density-functional perturbation theory (DFPT). For structures studied by QuantumEspresso v6.1,[4] geometry convergence was accepted with SCF convergence of 1.0×10^{-13} Ry, a total energy convergence of 1×10^{-10} Ry. Norm-conserving pseudopotentials were used in each case.

Table S1: Computational Parameters for the azides studied in this work. The ICSD code, exchange-correlation functional (XC), quantum chemistry code (CASTEP, C; Quantum Espresso, Q), convergence criteria and kinetic energy cut-off (ECut) are all given.

Azide	ICSD Code	Code	XC	D(Energy) / eV.atom^{-1}	Max. Force / eV Å^{-1}	Max. Atomic Disp. /Å	Max. Stress GPa	ECut /eV
NaN$_3$	29370	C	PBE + D2	2x10^{-6}	0.001	0.001	0.005	1800
NH$_4$N$_3$	2236	C	PBE +TS	2x10^{-6}	0.001	0.001	0.005	1800
TAGZ	Ref 5	C	PBE + TS	2x10^{-6}	0.001	0.001	0.005	1800
HN$_3$	261955	C	PBE + TS	2x10^{-6}	0.001	0.001	0.005	1800
LiN$_3$	34675	Q	rVV10	1x10^{-9}	1.0 x 10^{-8} Ry/Bohr	0.0001	5x10^{-6}	2312.9
Zn(N$_3$)$_2$	430428	C	PBE+D2	2x10^{-9}	0.0005	0.0005	0.0005	1800
Ba(N$_3$)$_2$	26202	Q	rVV10	1x10^{-9}	1.0 x 10^{-8} Ry/Bohr	0.0001	5x10^{-6}	2312.9
AgN$_3$	88335	Q	rVV10	1x10^{-9}	1.0 x 10^{-8} Ry/Bohr	0.0001	5x10^{-6}	1768.7
Sn(N$_3$)$_2$	433812	C	PBE + TS	2x10^{-6}	0.001	0.001	0.005	1800

S1.2 Comparison of Optimised Structures with Experimental Structures

As a means to benchmark the models used in this work, all computed structures are compared with experimental crystal structures. In all cases the optimised unit cell was found to adhere very closely to experimentally determined structures.

Table S1.2.1: Comparison of experimental (exp) and computed (calc) unit cell geometries.

Azide	a	b	c	α	β	γ	V	% Vol deviation
AgN$_3$ (Exp)	5.600	5.980	5.998	90.0	90.0	90.0	200.861	
AgN$_3$ (Calc)	5.717	5.962	5.979	90.0	90.0	90.0	203.815	+1.5
BaN$_3$ (Exp)	9.59	4.39	5.42	90.0	99.75	90.0	224.89	
BaN$_3$ (Calc)	9.826	4.444	5.532	90.0	99.14	90.0	238.50	+6
HN$_3$ (Exp)	8.208	8.208	6.782	110.42	110.42	90.01	397.42	
HN$_3$ (Calc)	8.381	8.381	6.903	110.51	110.51	90.00	421.18	+5.9
NH$_4$N$_3$ (Exp)	8.933	3.808	8.661	90.0	90.0	90.0	294.62	
NH$_4$N$_3$ (Calc)	9.016	3.814	8.573	90.0	90.0	90.0	294.80	+0.1

LiN$_3$ (Exp)	5.627	3.319	4.979	90.0	107.4	90.0	88.73	-0.005
LiN$_3$ (Calc)	5.594	3.323	4.911	90.0	104.8	90.0	88.25	
NaN$_3$ (Exp)	6.223	3.651	5.336	90.0	108.4	90.0	115.04	-0.4
NaN$_3$ (Calc)	6.161	3.685	5.198	90.0	103.8	90.0	114.61	
SnN$_3$ (Exp)	6.776	11.059	6.232	90.0	94.67	90.0	465.51	+0.7
SnN$_3$ (Calc)	6.686	11.795	5.948	90.0	91.41	90.0	468.93	
ZnN$_3$ (Exp)	3.459	16.261	6.931	90.0	95.9	90.0	387.8	+1.5
ZnN$_3$ (Calc)	3.439	16.469	6.997	90.0	96.42	90.0	393.84	

S2. CRYSTAL17 Computational Methods

The electronic structures of the crystalline azides were calculated using CRYSTAL17.[6] For all azides, the nitrogen atoms were treated using a triple-zeta with polarised valence basis set.[7] SCF convergence tolerance of 1 x 10^{-7} Ha was used, with integral tolerances of 7, 7, 7, 19, and 30 and TOLDEE 8. The basis sets, shrinking factors and resulting number of K-points are given in Table S2.1.

Table S2.1: Calculation parameters for CRYSTAL17 electronic structure calculations.

Azide	Counter Ion BS	SHRINK	Num K-point in IBZ
NaN$_3$	TZVP[7]	20	4004
NH$_4$N$_3$	5-11G* [8]	20	1331
TAGZ	C: 6-31d1G[9] H: TZVP[7]	15	1688
LiN$_3$	TZVP[7]	20	4004
HN$_3$	5-11G* [8]	15	1688
Zn(N$_3$)$_2$	4-11d31G [10]	20	2222
Ba(N$_3$)$_2$	HAYWSC-3111(2d)G [11]	20	2222
AgN$_3$	From Ref [12]	10	504
Sn(N$_3$)$_2$	DURAND-21G* [13]	20	2222

S3. Phonon Calculations

S3.1 Phonon Calculation Parameters

Phonon calculations were performed using the same computational packages as outlined in Section S1. For structures calculated using the CASTEP v16.1 code, dynamical matrices were initially calculated on a coarse grid (q-point spacing < 0.05 Å^{-1}), and subsequently Fourier interpolated onto a finer grid. The acoustic sum rule was implemented in reciprocal space. For those calculated within the QuantumESPRESSO v 6.1 package, phonon calculations were performed using the ph.x routine, within the framework of DFPT. Self-consistency threshold of 1x10^{-15} Ry was used in each case. The 'crystal' acoustic sum rule was implemented. A coarse grid was selected with q-point spacing <0.05 Å^{-1} in each case, followed by interpolation along a dense sent of q-points along all high symmetry paths in the Brillouin zone, as suggested by Ref [14], to no less than a total of 50 q-pts. For a few cases, considerably larger q-point integrations were attempted, and found to make negligible difference to the integration of $\Omega^{(2)}(\omega_T)$, Section S8.1.

S3.2 Phonon Dispersion Curves

The phonon dispersion curves were generated for each of the azide materials, Figures S3.2.1-S3.2.9. In each case, the target frequencies (main text, Table 3) are found to be relatively flat, while the phonon bands show large dispersion.
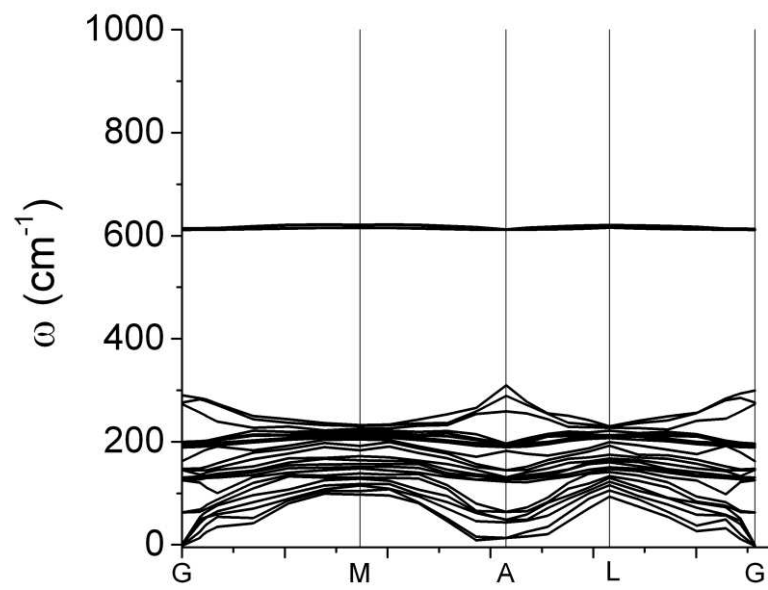
Fig S3.2.1: Phonon dispersion curve along the high symmetry paths for NaN$_3$.
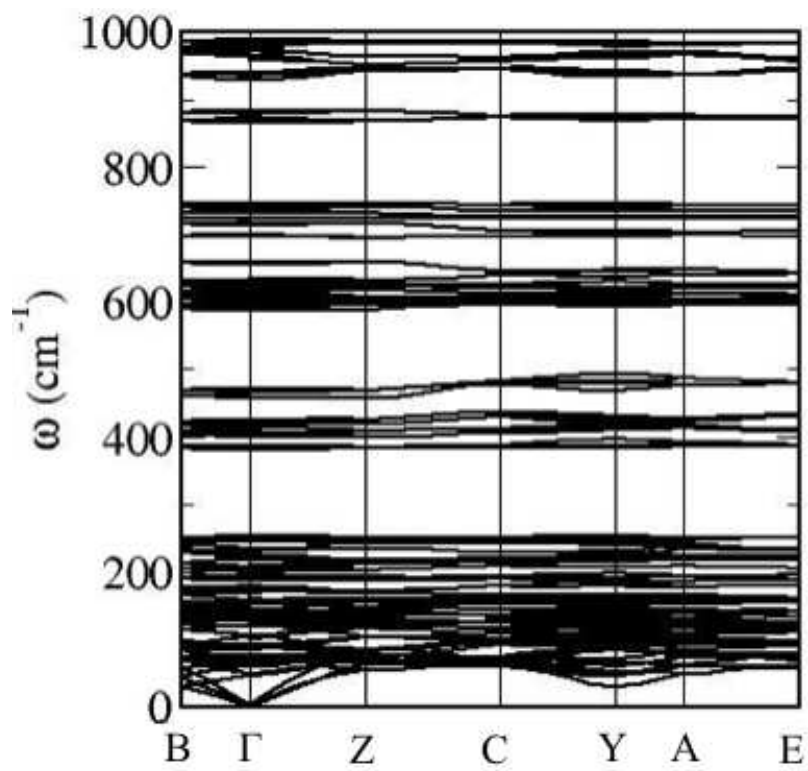

Fig S3.2.2: Phonon dispersion curve along the high symmetry paths for TAGZ.

Fig S3.2.3: Phonon dispersion curve along the high symmetry paths for NH_4N_3.

Fig S3.2.4: Phonon dispersion curve along the high symmetry paths for LiN_3.

Fig S3.2.5: Phonon dispersion curve along the high symmetry paths for HN_3

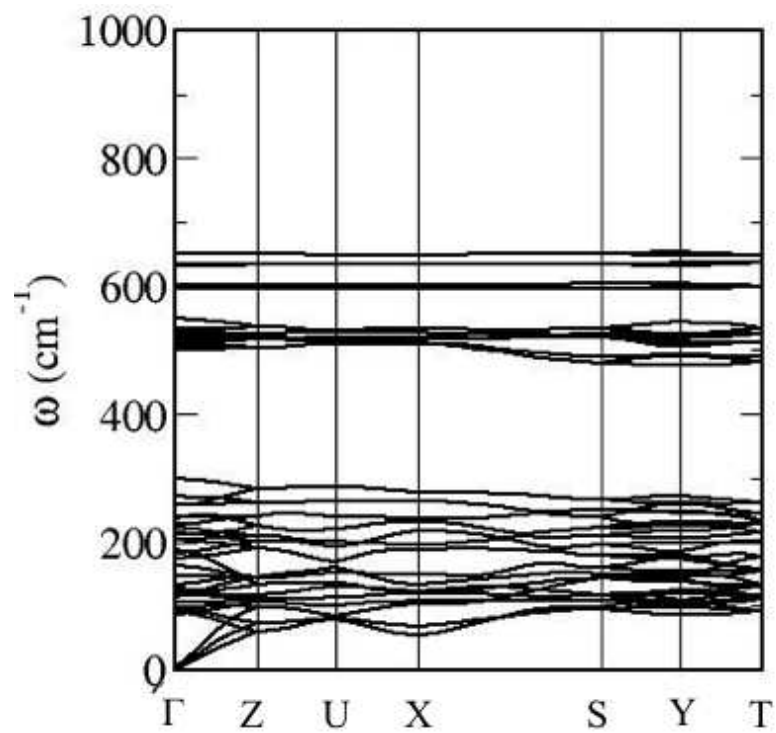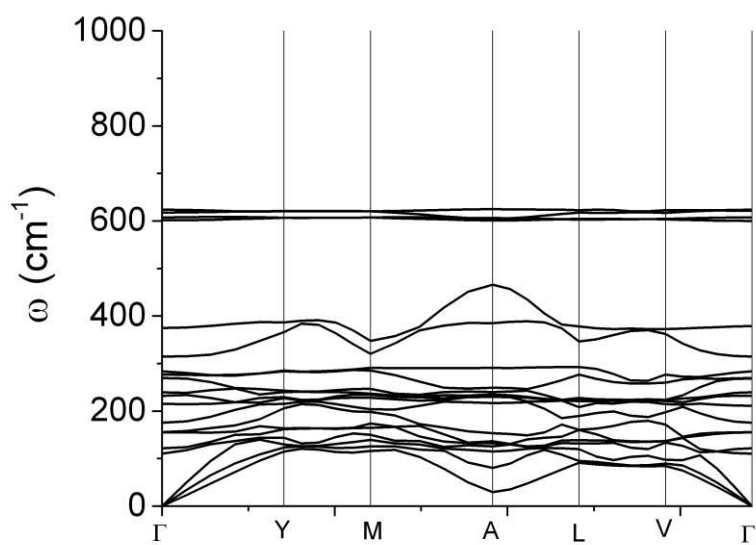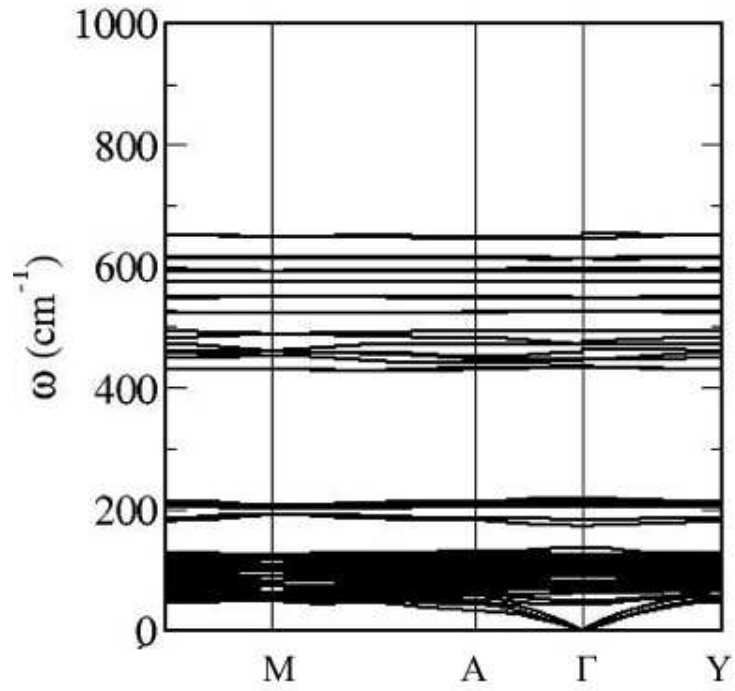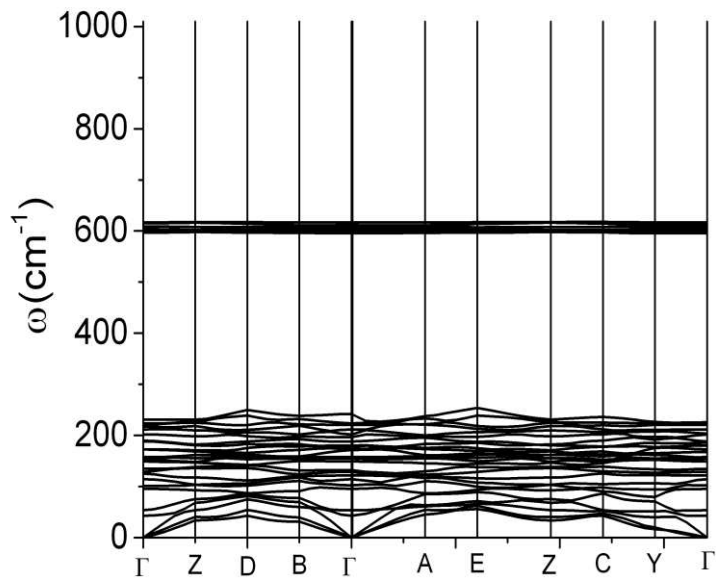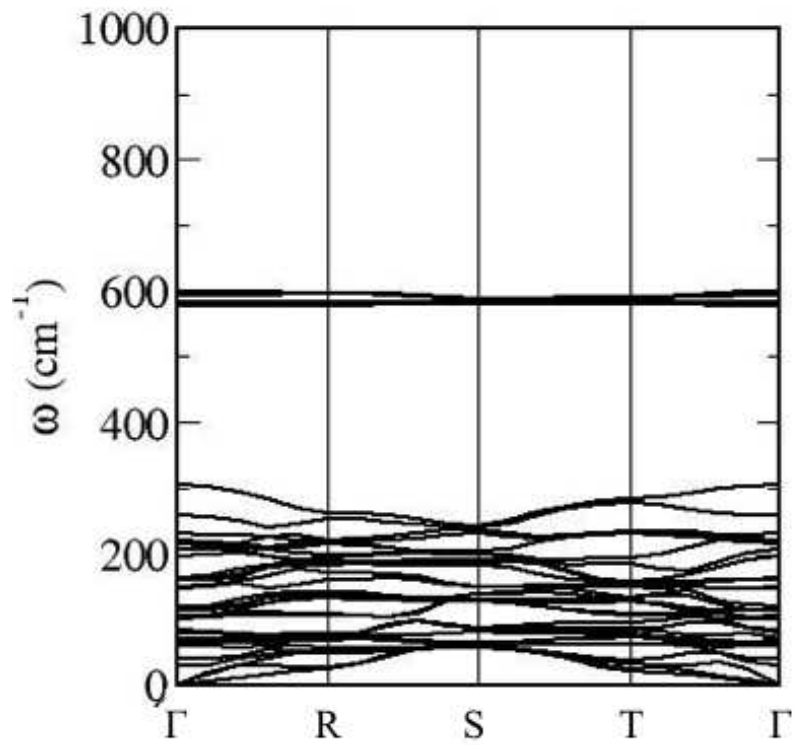Fig S3.2.6: Phonon dispersion curve along the high symmetry paths for $Ba(N_3)_2$.

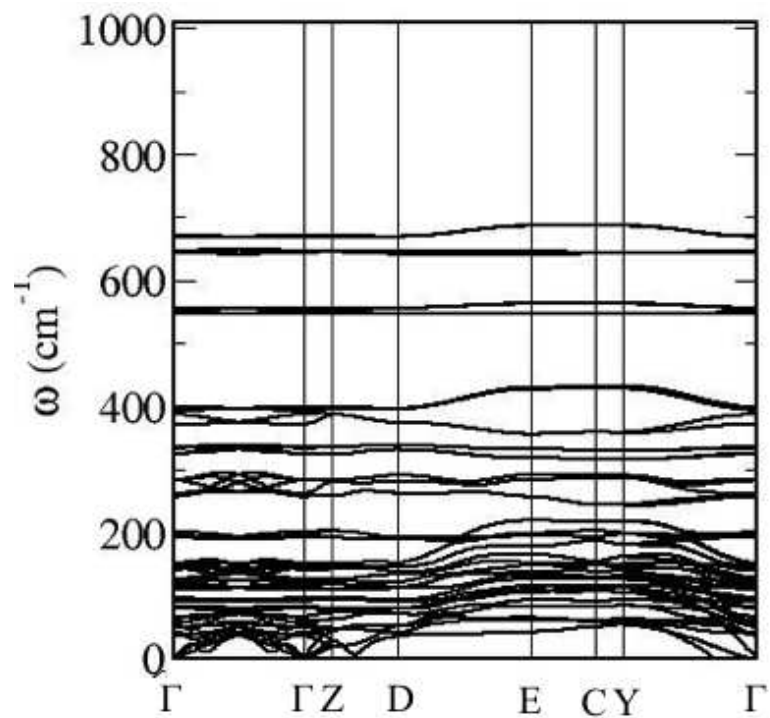Fig S3.2.7: Phonon dispersion curve along the high symmetry paths for AgN_3.

Fig S3.2.8: Phonon dispersion curve along the high symmetry paths for $Zn(N_3)_2$.
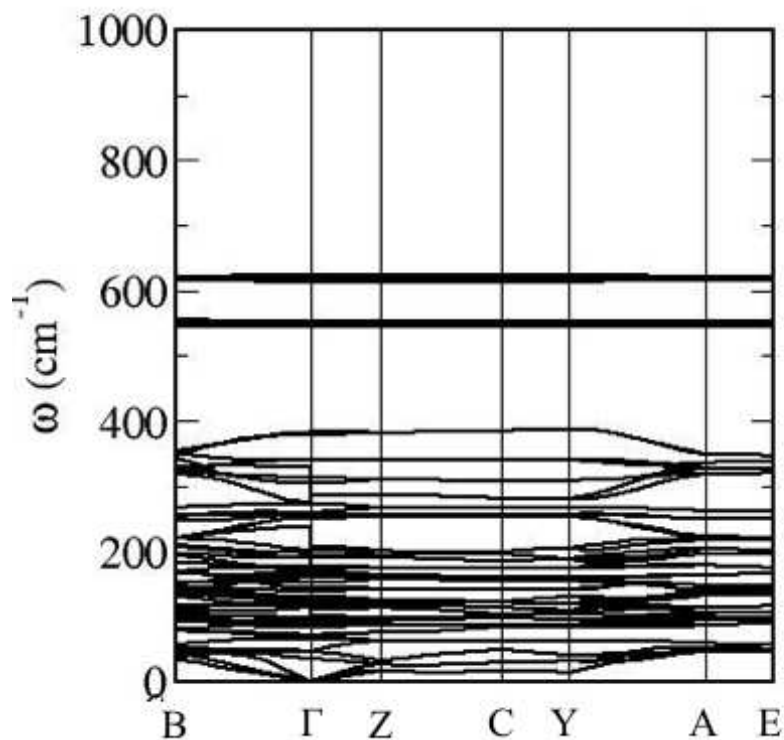
Fig S3.2.9: Phonon dispersion curve along the high symmetry paths for $Sn(N_3)_2$.

S4. Analysis of N-N interactions in Crystalline Azides (COHP)

Analysis of the projected Crystal overlap Hamilton population (pCOHP) was used to investigate the electronic structure of the N_3^- anion within the crystalline azides. In the main text, analysis is performed for the NaN_3 and AgN_3 systems: a non-covalent and a covalent system, respectively. Similar analysis has been performed for the remaining azides, which are presented in Figs S4.1-S4.6. The crystal canonical orbitals are also analysed in order to assist in the interpretation of the pCOHP. All pCOHP were generated using the HSE06 functional with minimum STO-3G basis set. Note that no suitable minimum basis set was available for $Ba(N_3)_{2,}$, and its analysis is therefore not presented here.

For the ionic azides (NaN_3, TAGZ, NH_4N_3, LiN_3) pCOHP analysis of the N_3^- molecule in the crystalline state shows the same electronic structure as presented for the isolated anion in the main text, Figure 2. As the interaction with the counter cation becomes increasingly covalent in nature, notable hybridisation of the N_3^- canonical orbitals is observed. This is generally accompanied by an increase in the anti-bonding character of the individual N...N bonds within the anion. However, we note that in each case, the underlying N_3^- orbitals can be generally recovered.

Fig S4.1: pCOHP analysis of N...N bonds in TAGZ. The crystalline canonical orbitals are given for selected features in the pCOHP curves. Symmetry classifications are based on the isolated N_3^- anion, and are used to reflect similarities with the pure anion.

Fig S4.2: pCOHP analysis of N...N bonds in NH_4N_3. The crystalline canonical orbitals are given for selected features in the pCOHP curves. Symmetry classifications are based on the isolated N_3^- anion, and are used to reflect similarities with the pure anion.
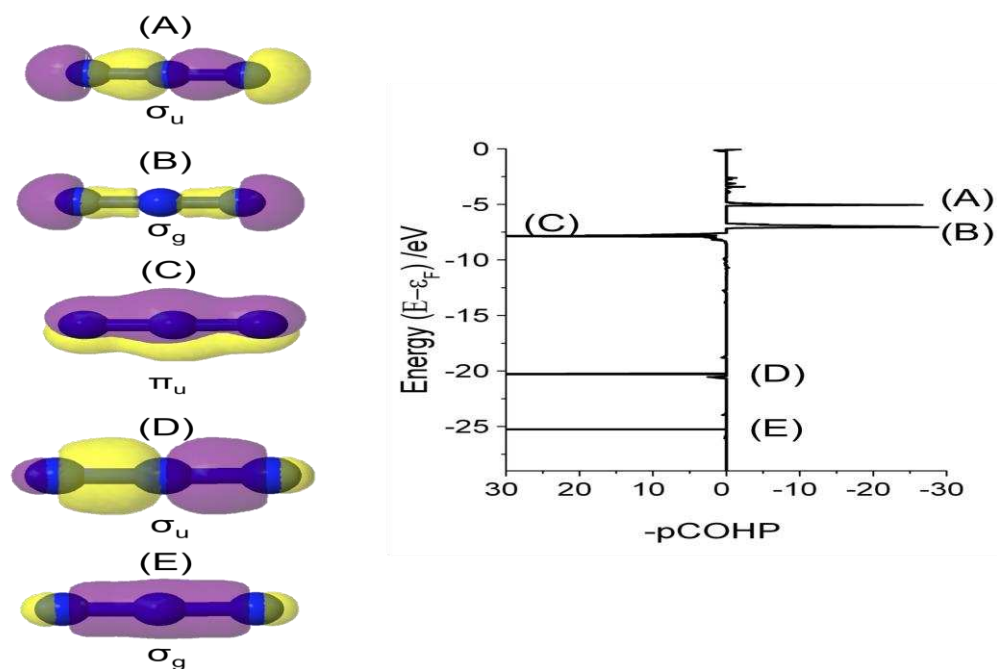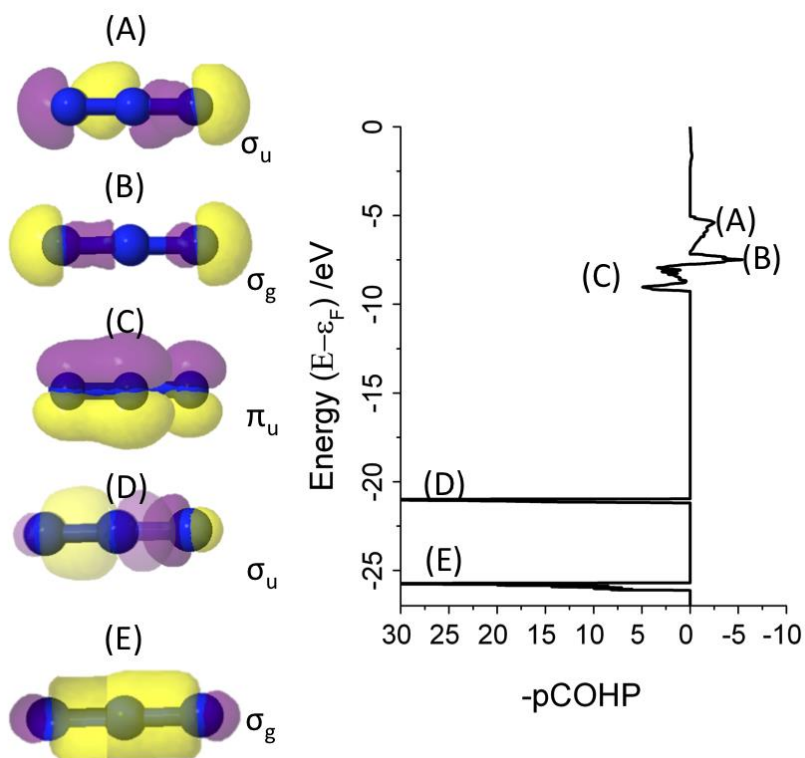
Fig S4.3: pCOHP analysis of N…N bonds in LiN$_3$. The crystalline canonical orbitals are given for selected features in the pCOHP curves. Symmetry classifications are based on the isolated N$_3^-$ anion, and are used to reflect similarities with the pure anion. Note orbitals were manually reconstructed across the periodic boundaries.
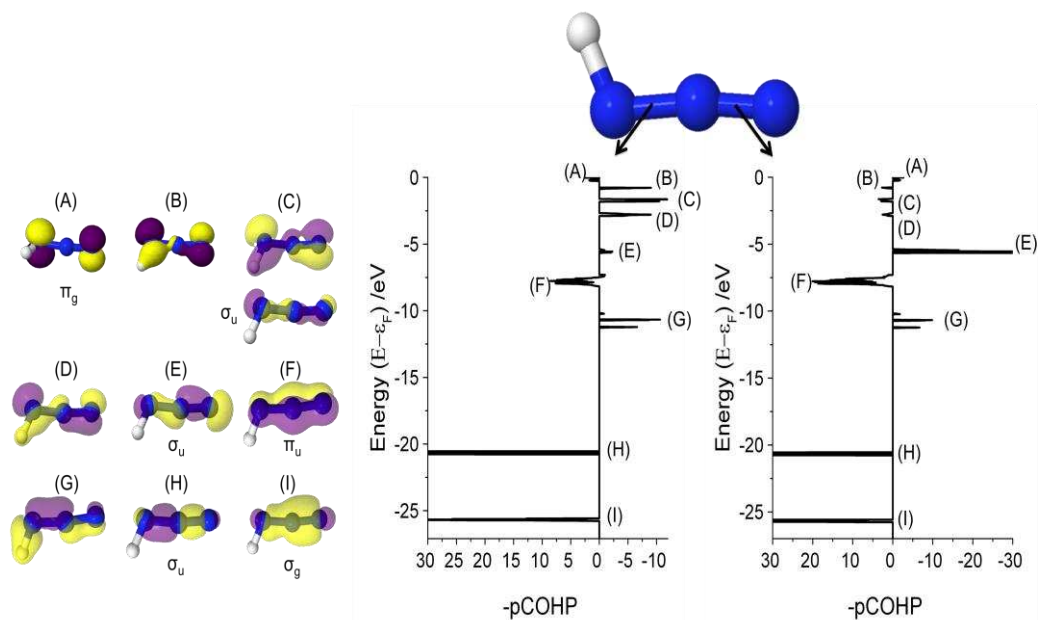
Fig S4.4: pCOHP analysis of HN$_3$ across the indicated N…N bonds. The crystalline canonical orbitals are given for selected features in the pCOHP curves. Symmetry classifications are based on the isolated N$_3^-$ anion, and are used to reflect similarities with the pure anion.
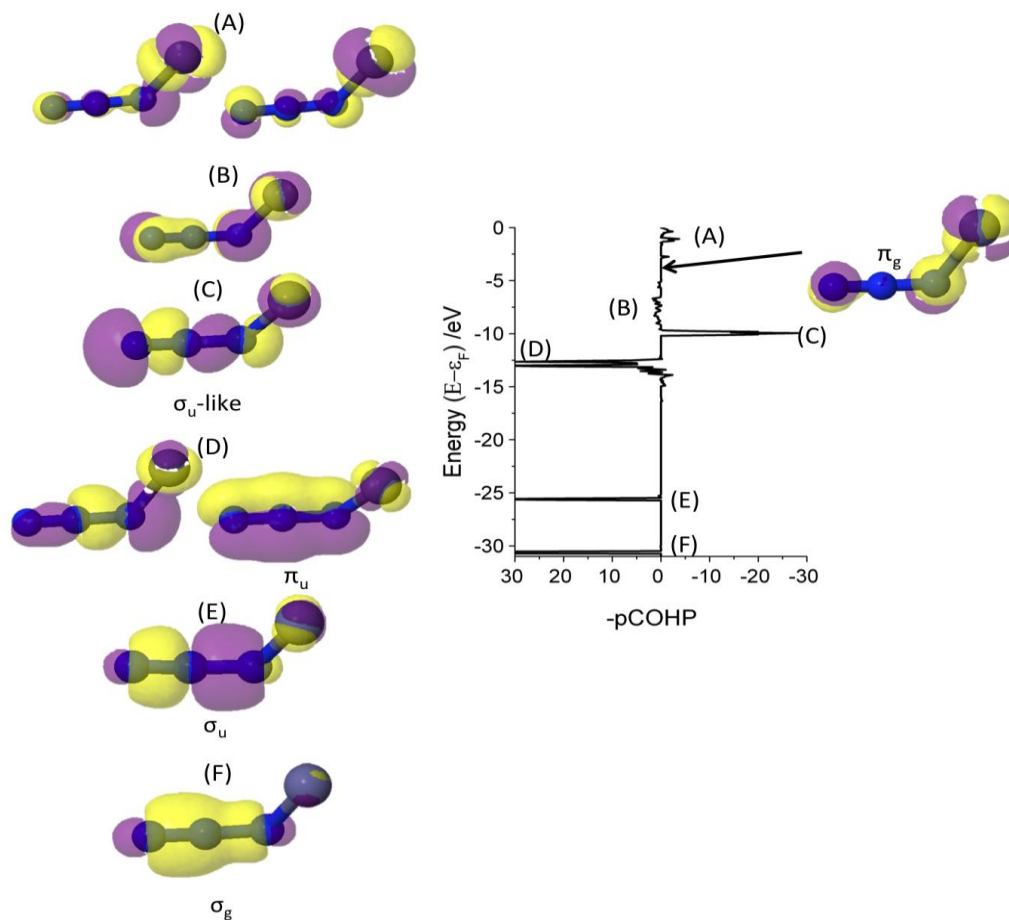
Fig S4.5: pCOHP analysis of N…N bonds in $Zn(N_3)_2$. Both N…N bonds exhibit the same major features. The crystalline canonical orbitals are given for selected features in the pCOHP curves. Symmetry classifications are based on the isolated N_3^- anion, and are used to reflect similarities with the pure anion.
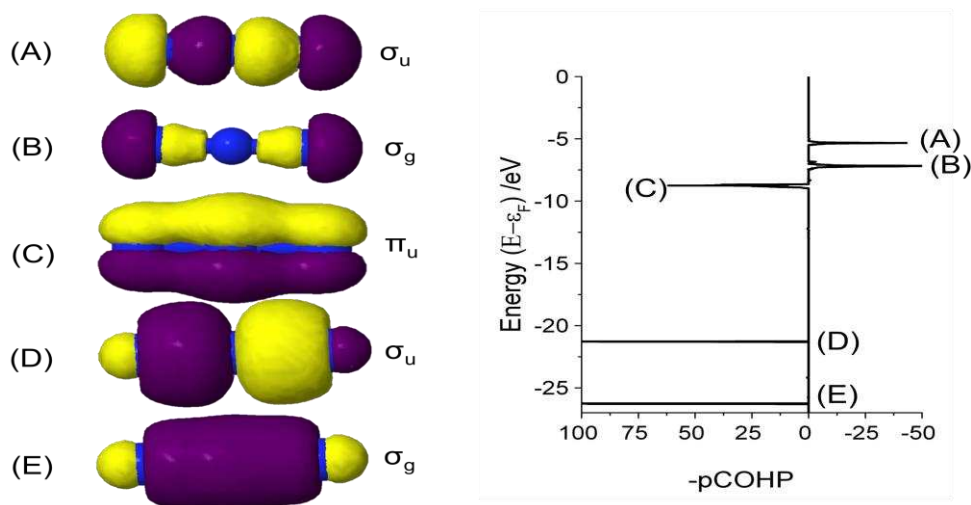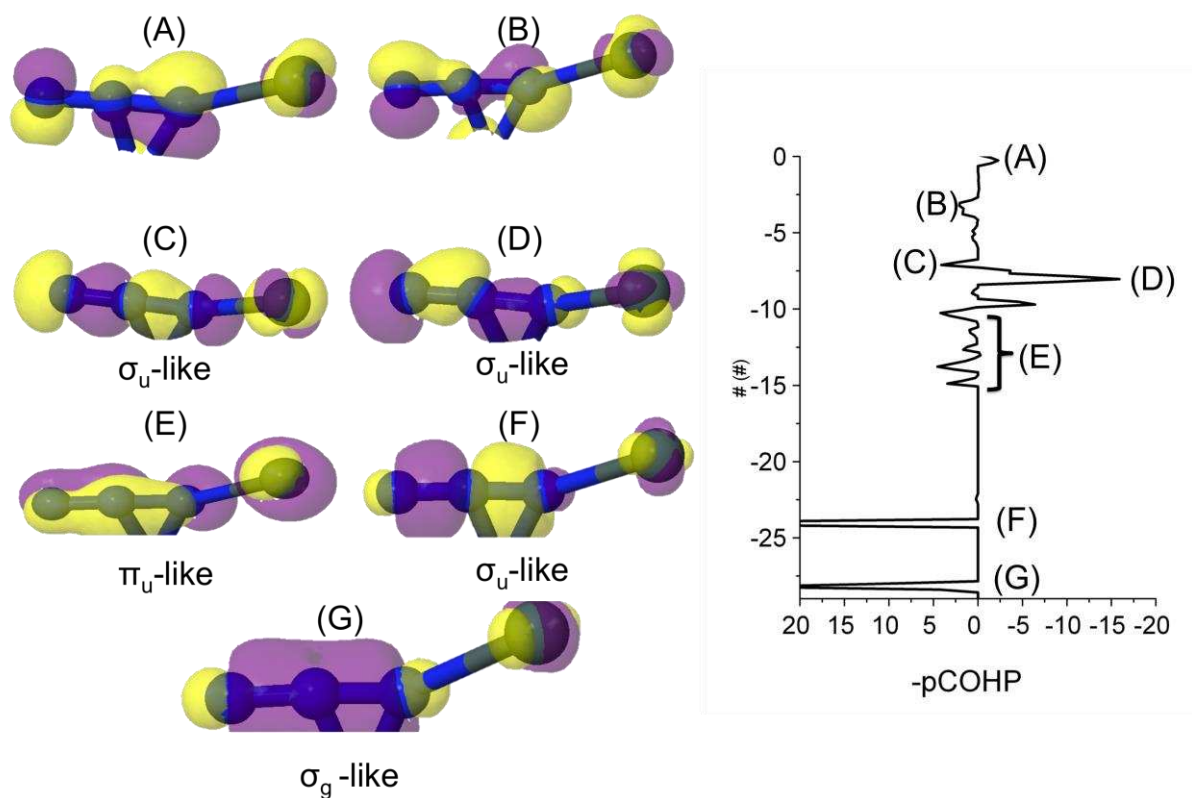
Fig S4.6: pCOHP analysis of N…N bonds in $Sn(N_3)_2$. The crystalline canonical orbitals are given for selected features in the pCOHP curves. Symmetry classifications are based on the isolated N_3^- anion, and are used to reflect similarities with the pure anion.

S5. Identification of Target Frequencies

In order to identify which vibrational modes correspond to θ_{NNN}, the Γ-point eigenvectors were analysed for each normal mode. Eigenvectors were artificially extended to accentuate internal molecular behaviour. The azide bend was therefore easily identified, Figure S5.1 Noting that the bands corresponding to each internal vibrational mode are relatively flat

means that the Γ-point frequencies are reliable indicators of the target frequency for each material.

Fig S5.1: Identification of target modes. The azide bend at each Γ-point normal mode is highlighted.

S6. Anharmonic mode coupling in LiN₃.

The solution of Equation 2 in the main text requires solution of the third-order scattering coefficients, $V^{(3)}$. This is, in principle, possible, and has been implemented in a variety of codes. Here, the D3Q code[15] has been used, as implemented for QuantumESPRESSO v6.1.

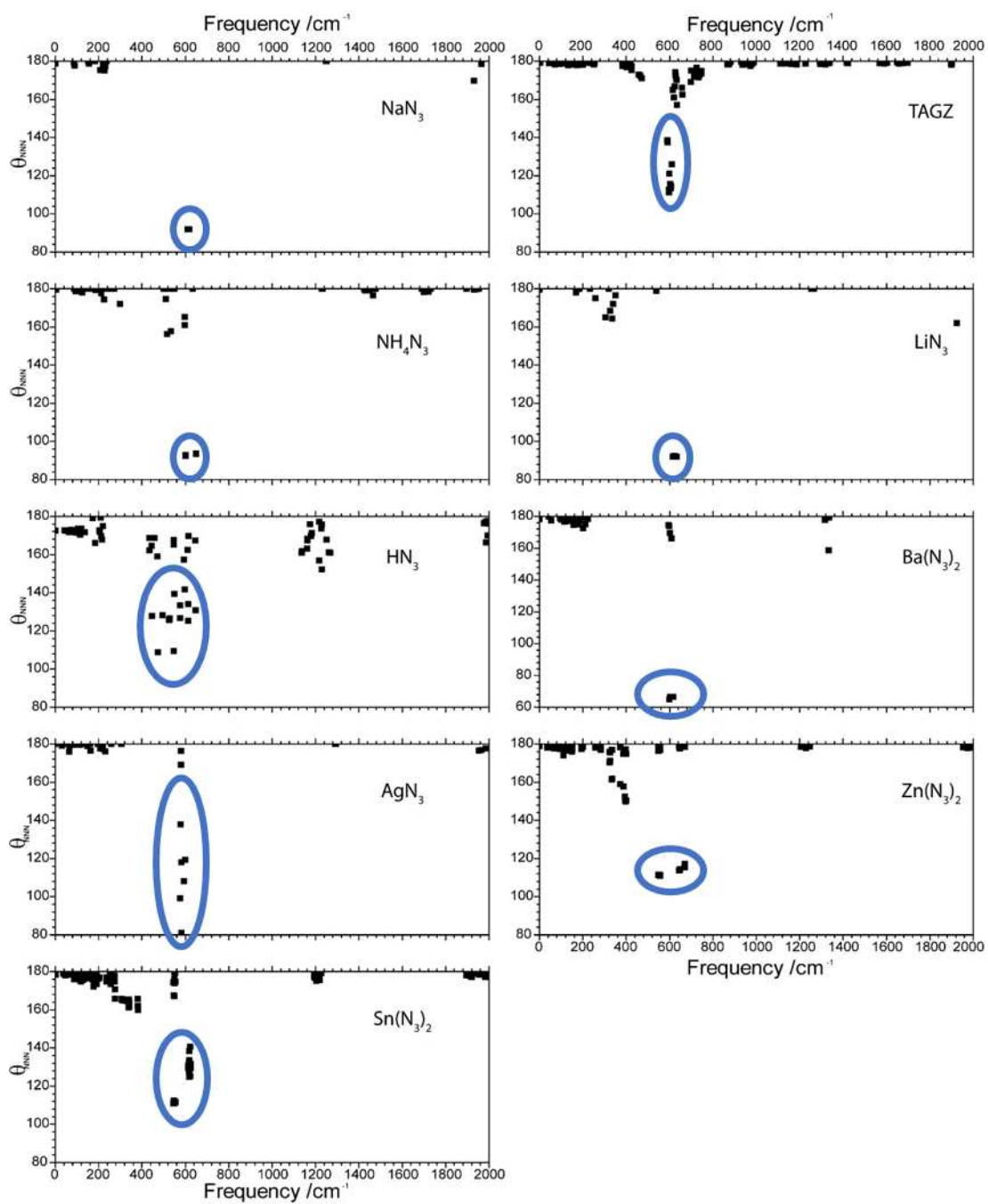Given the constraints on unit cell size, we were not able to compute the third order coupling matrix elements for either of the molecular salt azides (TAGZ or NH_4N_3). However, these calculations have been performed for LiN_3. We note that no single frequencies contained 'cation-only' modes, although Li-dominant modes were obvious (e.g. Γ-point *ca* 210, 220 and 230 cm^{-1}). Using the Γ-point vibrational mode at 602 cm^{-1} as the 'target' mode in the coupling calculations, the value of $V^{(3)}$ was calculated for zone-centre couplings, Table S6.1.

We note that there remains some strong coupling (although rare) with Li-dominant modes, e.g. 160/224 cm^{-1} coupling. However, we again stress that these modes retain azide character. It is clear that less azide character leads to considerably weaker (orders of magnitude) than for modes with strong azide character. It follows that for materials with strongly decoupled external modes (molecular salts), this difference in coupling strengths should be expected to be even larger.

Table S6.1: Cubic anharmonic coupling constants for zone-centre couplings to 602 cm^{-1} target mode in LiN_3. The coupling modes are labelled '1' and '2', and are indicated 'Li' if dominated by the Li cation.

Mode 1	Mode 2	Order of Magnitude Coupling Constant
160	134	E-16
160	100	E-38
160	150	E-38
160	210 (Li)	E-41
160	224 (Li)	E-12
160	232 (Li)	E-39
160	243	E-22
160	274	E-24
160	280	E-14
160	283	E-11
210 (Li)	134	E-34
210 (Li)	150	E-15
210(Li)	160	E-34
210(Li)	224 (Li)	E-34
210 (Li)	232(Li)	E-21
210 (Li)	243	E-34
210 (Li)	274	E-39
210((Li)	280	E-38
210(Li)	283	E-38
210(Li)	303	E-35

S7. Integration Window Effect

Due to slight broadening, minor errors associated with vibrational frequency calculations, Gaussian broadening in production of the PDOS, and to account for resonance between neighbouring state, an integration window was used to include density $\pm\omega_T$. In the main text, an integration window of $\omega_T \pm 10$ cm^{-1} was employed, as this reflects the Gaussian broadening applied in generation of the PDOS. To ensure no artificial ordering was introduced, the integration window was varied, Figure S7.1. The relative ordering remains the same in all cases, barring HN$_3$, whose integration window (435-500 cm^{-1}) is not affected by the choice of window. However, we note that the total integral of HN$_3$ is *ca* 13.5. The sensitivity ordering HN$_3$ > AgN$_3$ remains for all integration windows < $\pm$ 20.
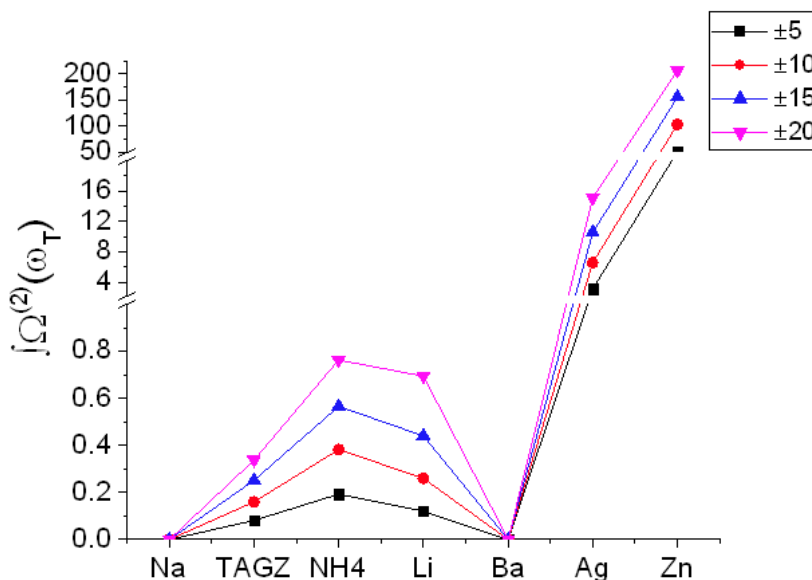

Fig S7.1: Effect of integration window on ordering of sensitivity

S8 Integration of multi-phonon Density of States

On examples tested, an increase in the fine grid used to produce the phonon density of states had negligible effect on the resulting integration of the two-phonon density of states. For example Zn(N$_3$)$_2$ PDOS generated using 8 q-points resulted in a $\Omega^{(2)}(\omega_T)$ = 102.57. Increasing the number of fine q-points to 420 resulted in $\Omega^{(2)}(\omega_T)$ = 102.8.

The integration values associated with Figure 8 in the main text are given in Table S8.1.

Table S8.1: Values for the integration of $\Omega^{(2)}(\omega_T \pm 10)$ for each azide. Values correspond to the data presented in the main text, Figure 8.

Azide	$\Omega^{(2)}$	
	Fig 8 A	Fig 8 B
NaN$_3$	0.01	0.34
TAGZ	0.16	0.27
NH$_4$N$_3$	0.39	0.71
LiN$_3$	0.28	0.81
HN$_3$	13.58	13.77
Ba(N$_3$)$_2$	0.01	1.41
AgN$_3$	6.11	7.63
Zn(N$_3$)$_2$	99.25	102.57
Sn(N$_3$)$_2$	23.57	26.48

REFERENCES

(1)   Clark, S. J.; Segall, M. D.; Pickard, C. J.; Hasnip, P. J.; Probert, M. I. J.; Refson, K.; Payne, M. C. First Principles Methods Using CASTEP. *Zeitschrift für Krist.* **2005**, *220* (5-6–2005), 567–570.

(2)   Perdew, J. P.; Burke, K.; Ernzerhof, M. Generalized Gradient Approximation Made Simple. *Phys. Rev. Lett.* **1996**, *77* (18), 3865–3868.

(3)   Pack, J. D.; Monkhorst, H. J. "special Points for Brillouin-Zone Integrations"-a Reply. *Phys. Rev. B* **1977**, *16* (4), 1748–1749.

(4)   Giannozzi, P.; Baroni, S.; Bonini, N.; Calandra, M.; Car, R.; Cavazzoni, C.; Ceresoli, D.; Chiarotti, G. L.; Cococcioni, M.; Dabo, I.; et al. QUANTUM ESPRESSO: A Modular and Open-Source Software Project for Quantum Simulations of Materials. *J. Phys. Condens. Matter* **2009**, *21* (39).

(5)   Bracuti, A. J.; Extine, M. W. 1,2,3-Triaminoguanidinium Azide (TAZ) Structure. *J. Crystallogr. Spectrosc. Res.* **1990**, *20* (1), 31–35.

(6)   Dovesi, R.; Orlando, R.; Erba, A.; Zicovich-Wilson, C. M.; Civalleri, B.; Casassa, S.; Maschio, L.; Ferrabone, M.; De La Pierre, M.; D'Arco, P.; et al. CRYSTAL14: A Program for the Ab Initio Investigation of Crystalline Solids. *Int. J. Quantum Chem.* **2014**, *114* (19), 1287–1317.

(7)   Peintinger, M. F.; Oliveira, D. V.; Bredow, T. Consistent Gaussian Basis Sets of Triple-Zeta Valence with Polarization Quality for Solid-State Calculations. *J. Comput. Chem.* **2013**, *34* (6), 451–459.

(8)   Dovesi, R.; Ermondi, C.; Ferrero, E.; Pisani, C.; Roetti, C. Hartree-Fock Study of Lithium Hydride with the Use of a Polarizable Basis Set. *Phys. Rev. B* **1984**, *29* (6), 3591–3600.

(9)   Gatti, C.; Saunders, V. R.; Roetti, C. Crystal Field Effects on the Topological Properties of the Electron Density in Molecular Crystals: The Case of Urea. *J. Chem. Phys.* **1994**, *101* (12), 10686–10696.

(10)   Jaffe, J. E.; Hess, A. C. Hartree-Fock Study of Phase Changes in ZnO at High Pressure. *Phys. Rev. B* **1993**, *48* (11), 7903–7909.

(11)   Zagorac, D.; Doll, K.; Schön, J. C.; Jansen, M. Sterically Active Electron Pairs in Lead Sulfide? An Investigation of the Electronic and Vibrational Properties of Pbs in the Transition Region between the Rock Salt and the α-GeTe-Type Modifications. *Chem. - A Eur. J.* **2012**, *18* (35), 10929–10936.

(12)   Doll, K.; Pyykkö, P.; Stoll, H. Closed-Shell Interaction in Silver and Gold Chlorides. *J. Chem. Phys.* **1998**, *109* (6), 2339–2345.

(13)   Causà, M.; Dovesi, R.; Roetti, C. Pseudopotential Hartree-Fock Study of Seventeen III-V and IV-IV Semiconductors. *Phys. Rev. B* **1991**, *43* (14), 11937–11943.

(14)   Hinuma, Y.; Pizzi, G.; Kumagai, Y.; Oba, F.; Tanaka, I. Band Structure Diagram Paths Based on Crystallography. *Comput. Mater. Sci.* **2017**, *128*, 140–184.

(15)   Paulatto, L.; Mauri, F.; Lazzeri, M. Anharmonic Properties from a Generalized Third-Order Ab Initio Approach: Theory and Applications to Graphite and Graphene. *Phys. Rev. B - Condens. Matter Mater. Phys.* **2013**, *87* (21), 1–18.